

# Injection-Limited and Space-Charge-Limited Conduction in Wide Bandgap Semiconductors with Velocity Saturation Effect

Kok Wai Lee and Yee Sin Ang<sup>a)</sup>

Science and Math, Singapore University of Technology and Design, Singapore 487372

Carrier conduction in wide bandgap semiconductors (WBS) often exhibits velocity saturation at the high-electric field regime. How such effect influences the transition between contact-limited and space-charge-limited current in a two-terminal device remains largely unexplored thus far. Here, we develop a generalized carrier transport model that includes contact-limited field-induced carrier injection, space charge, carrier scattering and velocity saturation effect. The model reveals various transitional behaviors in the current-voltage characteristics, encompassing Fowler-Nordheim emission, trap-free Mott-Gurney (MG) SCLC and *velocity-saturated SCLC*. Using GaN, 6H-SiC and 4H-SiC WBS as examples, we show that the velocity-saturated SCLC completely dominates the high-voltage ( $10^2 \sim 10^4$  V) transport for typical sub- $\mu\text{m}$  GaN and SiC diodes, thus unravelling velocity-saturated SCLC as a central transport mechanism in WBG electronics.

Space-charge-limited current (SCLC) is the maximum current density which can be injected across a diode of channel length,  $D$  subjected to a bias voltage,  $V$ <sup>1</sup>. Very generally, SCLC can be described by the scaling law:

$$J \propto \frac{V^\alpha}{L^\beta} \quad (1)$$

whereby the scaling exponents  $\alpha$  and  $\beta$  are determined by the material properties and device geometry<sup>2</sup>. In a one-dimensional (1D) diode, SCLC can be broadly classified into ballistic and collisional types. The former occurs in vacuum whereby SCLC is governed by the Child-Langmuir (CL) law<sup>3,4</sup> with  $(\alpha, \beta) = (3/2, 2)$ . The latter occurs in solids such as semiconductors and insulators in which carrier scattering effects are present. Depending on the defect characteristics and device geometry<sup>5</sup>, the scaling factors  $(\alpha, \beta)$  can take the form of: (i) (3, 2) for the cases of trap-free, trap-filled, and traps with discrete energy level (i.e. Mott-Gurney (MG)<sup>6</sup>, Lampert<sup>7</sup> and Rose<sup>8</sup> models); (ii)  $(l + 1, 2l + 1)$  for a shallow exponential distribution of traps whereby  $l$  is a parameter related to trap characteristics and temperature (i.e. Mark-Helfrich (MH) model<sup>9</sup>); (iii) (3/3) and  $(l + 1, l + 1)$  for trap-free (trap-filled) and trap-limited ultrathin diode, respectively<sup>10,11</sup>; and (iv) (1/2, 1/2) for two-dimensional (2D) Dirac semiconductors<sup>12</sup>. Due to the sensitive dependence of SCLC current-voltage-length scaling on the material properties and device geometry, SCLC has been widely used as an effective *diagnostic tool* to probe the material properties (e.g. carrier mobility, trap density)<sup>13,14</sup>, and has been extensively used to investigate organic<sup>15</sup> and inorganic semiconductors<sup>16,17</sup>, metal halide perovskites<sup>14,18–20</sup>, dielectrics and wide bandgap (WBG) semiconductors<sup>21–25</sup>.

Modelling the transitions between various transport processes into SCLC is essential for device design and characterization of both vacuum as well as solid-state diodes and transistors. Various transitional behaviours

have been previously uncovered, including the transitions from contact-limited to space-charge-limited in the ballistic<sup>26</sup> and collisional<sup>27,28</sup> regimes, the inclusion of thermionic effect<sup>29</sup>, and the peculiar absence of SCLC in 2D materials<sup>30</sup>. It should be noted that prior transitional models<sup>27,28,30</sup> typically assume a *constant* carrier mobility, which is only approximately valid at the low-electric field regime. For most solids, the carrier mobility becomes field-dependent at higher field. In particular, in wide bandgap semiconductors (WBS), the field-dependent mobility can be described by the Caughey-Thomas mobility model<sup>31</sup> where the the charge carrier velocity saturates towards a maximum drift velocity, known as the *saturation velocity* ( $v_s$ )<sup>32–38</sup>, which arises from carrier scattering effects such as optical phonon scattering<sup>39</sup>. How velocity saturation affects and/or competes with SCLC (note that both occurs at high fields) and a general transport model encompassing contact-limited field emission, SCLC and velocity saturation effect remain open questions thus far.

In this work, we develop a generalized transport model that covers both contact-limited and space-charge-limited conduction regimes in the presence of carrier scattering and velocity saturation effects. By combining the carrier equation of motion, Caughey-Thomas mobility model and Poisson's equation, the current-voltage ( $J-V$ ) characteristics for both electron and hole transports are obtained, which enable the rich transitional behaviors between field emission (FE), trap-free Mott-Gurney SCLC (SCLC<sub>MG</sub>) and the velocity-saturated SCLC (SCLC<sub>VS</sub>) to be elucidated. We construct the nexus plots to illustrate various transitions under varying material/device parameters. Using the archetypal WBS of gallium nitride (GaN), and silicon carbide (SiC) polytypes of 6H-SiC and 4H-SiC, we show that the current-voltage curve transits directly from the contact-limited FE to SCLC<sub>VS</sub> while the SCLC<sub>MG</sub> commonly observed in dielectrics and insulators is completely absent, thus suggesting the importance of velocity saturation effect in WBS-based devices operating at high voltages.

The model developed here shall provide a theoretical basis for the modelling and analysis of WBS-based

<sup>a)</sup>Electronic mail: [yeesin.ang@sutd.edu.sg](mailto:yeesin.ang@sutd.edu.sg)

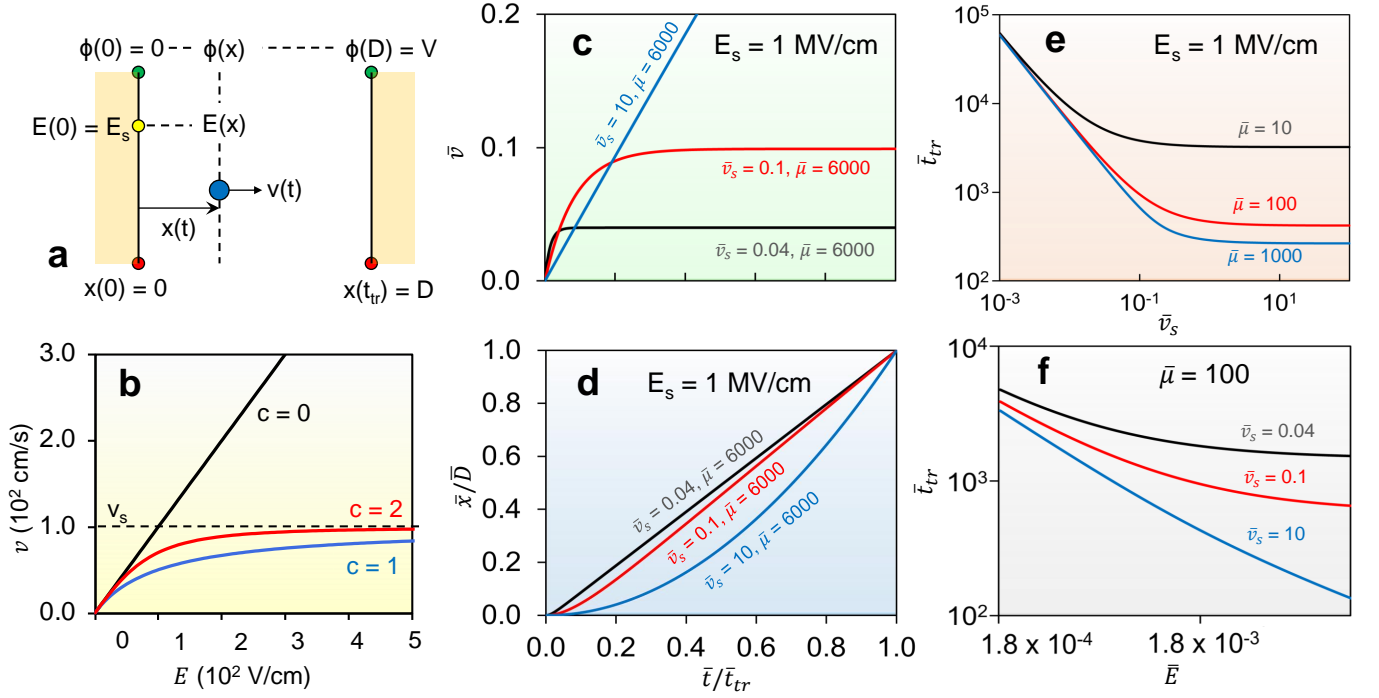


FIG. 1. (a) Schematic diagram of the 1D charge carrier transport. (b)  $v - E$  plot at  $v_s = 100$  cm/s for  $c = 0, 1$  and  $2$ . (c)  $\bar{v} - \bar{t}/\bar{t}_{tr}$  and (d)  $\bar{x}/D - \bar{t}/\bar{t}_{tr}$  plots at  $E_s = 1$  MV/cm for different  $\bar{v}_s$ . (e)  $\bar{t}_{tr} - \bar{v}_s$  plot at  $E_s = 1$  MV/cm for different  $\bar{\mu}$ . (f)  $\bar{t}_{tr} - \bar{E}$  plot at  $\bar{\mu} = 100$  for different  $\bar{v}_s$ . The device length is  $D = 100$  nm.

devices – a key building block of high-voltage/high-temperature electronics much sought-after for electric vehicles<sup>40</sup> and harsh environment applications<sup>41</sup>, and can also be used to investigate the effect of velocity saturation on vacuum diode with residual gas<sup>27,29</sup> as well as the breakdown phenomenon in micro/nanogap devices<sup>42,43</sup>.

We consider the one-dimensional (along the  $x$ -direction) charge carrier transport across a planar diode with the cathode located at  $x = 0$  and the anode located at  $x = D$  biased at a voltage,  $V$  with respect to the cathode as shown in Fig. 1(a). The position and velocity of the injected carrier are  $x(t)$  and  $v[x(t)]$  respectively. The local electric field at  $x$  is  $E[x(t)]$ . The carrier injected from the cathode into the diode bulk is assumed to have a zero initial ( $t = 0$ ) velocity,  $v$  and such injection is driven by the surface electric field,  $E_s$ , giving rise to the set of initial conditions  $x(0) = 0$ ,  $v(0) = 0$  and  $E(0) = E_s$ .

We first model the electrostatics and carrier transport by coupling Poisson's equation with the current density equation,  $J = n[x(t)]ev[x(t)]$  with  $n[x(t)]$  and  $e$  being the position-dependent carrier density and electric charge constant respectively. Thus, we obtain  $d^2\phi(x)/dx^2 = J/\epsilon v$  whereby  $\phi(x)$  is the electric potential and  $\epsilon$  is the dielectric constant of the diode channel<sup>44</sup>. By using the electric field  $E[x(t)] = d\phi[x(t)]/dx$  and carrier velocity  $v[x(t)] = dx(t)/dt$  relations, integration with respect to

$x$  yields

$$E[x(t)] = \frac{d\phi[x(t)]}{dx} = E_s + \frac{J(E_s)t}{\epsilon} \quad (2)$$

where we have used the initial condition of  $E[x(t)] = E_s$  at  $t = 0$ . The current flowing in the diode is determined by that injected from the cathode which can be described by the Fowler-Nordheim (FN) law,

$$J(E_s) = A_{FN}E_s^2 \exp\left(-\frac{B_{FN}}{E_s}\right) \quad (3)$$

whereby  $E_s$  is the surface electric field at the cathode, while  $A_{FN}$  and  $B_{FN}$  are the first and second FN constants.

Next, we derive the equation of motion (EOM) of a charge carrier traversing across the diode in the presence of carrier scattering or collisional effect. Such effect is captured by a friction term in the EOM<sup>27</sup>, i.e.

$$m \frac{dv[x(t)]}{dt} = eE[x(t)] - \alpha(E[x(t)])v[x(t)] \quad (4)$$

whereby  $\alpha(E[x(t)])$  is a 'friction-coefficient-like' term related to the strength of the collision, and is generally field-dependent. At steady state, Eq. (4) yields  $v[x(t)] = [e/\alpha(E[x(t)])]E[x(t)]$  where the carrier mobility can be written as  $\mu \equiv e/\alpha(E[x(t)])$  to yield the familiar expression of  $v[x(t)] = \mu E[x(t)]$ . The carrier mobility is approximately field-independent at the low-field regime

but acquires significant field-dependence at the high-field regime. Since SCLC is a high-field phenomenon, the inclusion of field-dependent carrier mobility is particularly important in the modelling of SCLC in solid-state diodes.

To incorporate the field-dependent collisional effect into the EOM, we consider the Caughey-Thomas carrier mobility model<sup>31</sup>:

$$\mu(E) = \frac{\mu_0 E}{\left[1 + \left(\frac{\mu_0 E}{v_s}\right)^c\right]^{\frac{1}{c}}} \quad (5)$$

whereby  $\mu_0$  is the low-field carrier mobility and we suppress the argument of  $E[x(t)]$  for notational simplicity. At the high-electric field regime of  $E \gg v_s/\mu_0$ , the carrier velocity approaches the saturation velocity  $v_s$  as shown in Fig. 1(b). The coefficient  $c$  is an experimental fit-

ting parameter generally equals to 1 (2) for holes (electrons). Nevertheless, the actual value may differ from 1 or 2 and is typically determined empirically from experimental data. For instance,  $c = 2$  is a suitable fitting value to be used to determine the saturation velocity of graphene on SiO<sub>2</sub><sup>45</sup> whereas  $c$  ranging from 2.8 to 4.8 are suitable fitting values to be used to determine a range of values for the saturation velocity of synthetic monolayer MoS<sub>2</sub><sup>36</sup>.  $v_s$  is material-dependent which is influenced by various factors such as temperature and doping density<sup>46,47</sup>. The value of  $v_s$  varies across different materials and could range from 10<sup>5</sup> cm/s to 10<sup>7</sup> cm/s. For instance, amorphous indium gallium zinc oxide (a-IGZO) has a saturation velocity of  $3.8 \times 10^5$  cm/s<sup>48</sup> whereas gallium arsenide (GaAs) has a much higher saturation velocity of  $1.2 \times 10^7$  cm/s.

Combining Eqs. (2), (4) and (5), we obtain the field-dependent EOM,

$$\frac{dv[x(t)]}{dt} = \frac{e}{m} \left(E_s + \frac{Jt}{\epsilon}\right) - \frac{e}{m\mu_0} v[x(t)] \left[1 + \frac{\mu_0}{v_s} \left(E_s + \frac{Jt}{\epsilon}\right)^c\right]^{1/c} \quad (6)$$

whereby  $m$  is the electron effective mass. For a given  $E_s$ , the injection current,  $J(E_s)$  is determined from Eq. (3). For any value of  $c$ , Eq. (6) can be solved numerically to yield the carrier velocity and position profiles,  $v(t)$  and  $x(t)$  respectively. The transit time,  $t_{tr}$  – time taken for a charge carrier to traverse across the diode – is obtained using the boundary condition,  $x(t_{tr}) = D$ . Integrating Eq. (6) yields

$$V(E_s) = \frac{1}{e} \frac{mv[x(t_{tr})]^2}{2} + \frac{1}{m\mu_0} \int_0^{t_{tr}} \left[1 + \frac{\mu_0}{v_s} \left(E_s + \frac{Jt}{\epsilon}\right)^c\right]^{1/c} v[x(t)]^2 dt \quad (7)$$

whereby  $V(E_s)$  is the bias voltage and we have used  $dx = vdt$  and Eq. (2) to obtain Eq. (7). Eq. (7) can be used to construct the current-voltage characteristics together with Eq. (3). For  $c = 1$ ,  $v(t)$  and  $x(t)$  can be solved for analytically from Eq. (6), yielding

$$\bar{v}(\bar{t}) = \bar{v}_s \left\{ 1 - \exp \left[ \frac{-\bar{t}(2\bar{v}_s + 2\bar{\mu}\bar{E} + \bar{\mu}\bar{J}\bar{t})}{2\bar{v}_s\bar{\mu}} \right] \right\} + \frac{\bar{v}_s^{\frac{3}{2}}}{\bar{\mu}} \sqrt{\frac{2}{\bar{J}}} \left\{ \exp \left[ \frac{-\bar{t}(2\bar{v}_s + 2\bar{\mu}\bar{E} + \bar{\mu}\bar{J}\bar{t})}{2\bar{v}_s\bar{\mu}} \right] F(\psi) - F(\gamma) \right\} \quad (8)$$

$$\begin{aligned} \bar{x}(\bar{t}) = & \bar{v}_s \bar{t} + \bar{v}_s^{\frac{3}{2}} \sqrt{\frac{\pi}{2\bar{J}}} \exp(\psi^2) [\operatorname{erf}(\psi) - \operatorname{erf}(\gamma)] + \frac{\pi \bar{v}_s^2}{2\bar{\mu}\bar{J}} \operatorname{erfi}(\psi) [-\operatorname{erf}(\psi) + \operatorname{erf}(\gamma)] \\ & - \frac{\bar{v}_s^{\frac{3}{2}}}{\bar{\mu}} \sqrt{\frac{\pi}{2\bar{J}}} \left\{ -\frac{\bar{v}_s(\bar{v}_s + \bar{\mu}\bar{E})^2 {}_2F_2(1, 1; \frac{3}{2}, 2; -\psi^2)}{\bar{\mu}^2 \sqrt{2\pi}(\bar{v}_s\bar{J})^{\frac{3}{2}}} + \frac{\bar{v}_s[\bar{v}_s + \bar{\mu}(\bar{J}\bar{t} + \bar{E})]^2 {}_2F_2(1, 1; \frac{3}{2}, 2; -\gamma^2)}{\bar{\mu}^2 \sqrt{2\pi}(\bar{v}_s\bar{J})^{\frac{3}{2}}} \right\} \end{aligned} \quad (9)$$

whereby

$$\psi = \frac{\bar{v}_s + \bar{\mu}\bar{E}}{\bar{\mu}\sqrt{2\bar{J}\bar{v}_s}}; \quad \gamma = \frac{\bar{v}_s + \bar{\mu}(\bar{E} + \bar{J}\bar{t})}{\bar{\mu}\sqrt{2\bar{J}\bar{v}_s}}. \quad (10)$$

Here  $F(x)$  is Dawson's integral<sup>49</sup>,  $\operatorname{erf}(x)$  and  $\operatorname{erfi}(x)$  are the error and imaginary error functions respectively and  ${}_2F_2(a_1, a_2; b_1, b_2; z)$  is the generalized hypergeometric function of order  $p = q = 2$ . The normalisation terms<sup>27,29</sup> are defined as:  $\phi = \phi_0\bar{\phi}$ ,  $J = J_0\bar{J}$ ,  $x = x_0\bar{x}$ ,  $t = t_0\bar{t}$ ,  $\mu = \mu_0\bar{\mu}$ ,  $E = E_0\bar{E}$ ,  $v = v_0\bar{v}$ ,  $v_s = v_0\bar{v}_s$  whereby  $\phi_0 = e\epsilon_0^2/mA_{FN}^2$ ,  $J_0 = A_{FN}B_{FN}^2$ ,  $x_0 = e\epsilon_0^2/mA_{FN}^2B_{FN}$ ,  $t_0 = \epsilon_0/A_{FN}B_{FN}$ ,  $\mu_0 = e\epsilon_0/mA_{FN}B_{FN}$ ,  $E_0 = B_{FN}$  and  $v_0 = x_0/t_0$ . In the large- $v_s$  regime, Eqs. (8) and (9) reduce to the collisional model of Darr et al<sup>27</sup>. More interestingly, at large  $J$ , Eq. (7) becomes  $V \rightarrow (v_s/2m\epsilon)t_{tr}^2$  where  $t_{tr} \rightarrow D/v_s$  approaches the time taken to traverse across the channel by a constant saturation velocity  $v_s$ . This leads to the velocity-saturated SCLC (SCLC<sub>VS</sub>) of  $J_{VS} = 2\epsilon v_s V/D^2$ <sup>50</sup> which, as demonstrated below, dominates the high-voltage transport in WBS-based devices.

Fig. 1(b) shows the carrier velocity as a function of  $E$  for three different values of  $c$ . For  $c = 0$ , the velocity

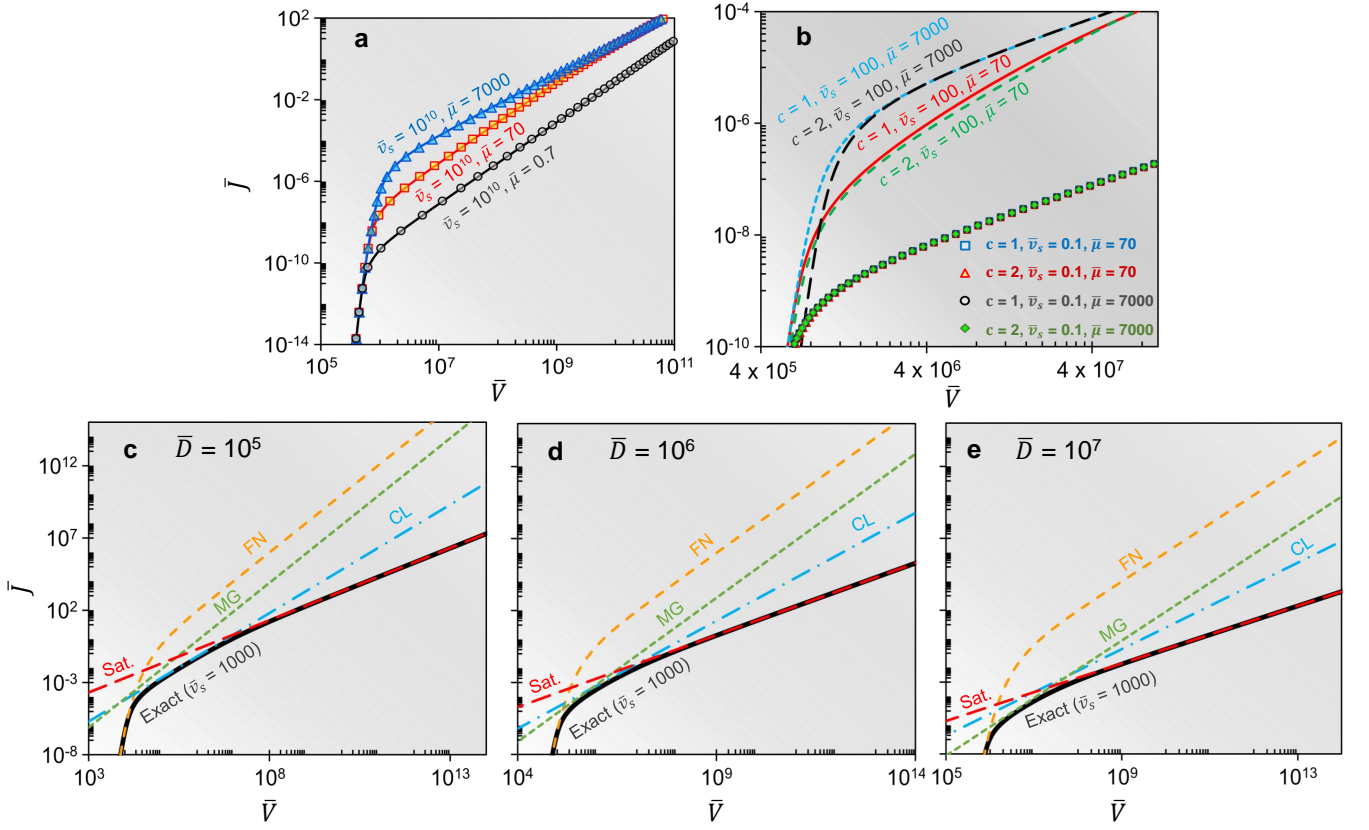


FIG. 2. (a) Comparison between  $\bar{J} - \bar{V}$  characteristic curves obtained by our model with  $c = 1$  (markers) and obtained by Darr et al<sup>27</sup> (solid lines) for  $\bar{\mu} = 0.7, 70$  and  $7000$  at  $\bar{D} = 10^7$ . (b) Comparison between  $\bar{J} - \bar{V}$  characteristic curves for  $c = 1$  and  $2$  at  $\bar{D} = 10^7$  for different  $\bar{\mu}$  and  $\bar{v}_s$ .  $\bar{J} - \bar{V}$  characteristic curves at  $\bar{\mu} = 700$  for (c)  $\bar{D} = 10^5$ , (d)  $\bar{D} = 10^6$  and (e)  $\bar{D} = 10^7$ .

saturation effect is absent and a  $v - E$  linear relationship is obtained. For both  $c = 1$  and  $2$ , the curves approach the saturation velocity of  $100$  cm/s as  $E$  increases. In this case, the curve of  $c = 2$  reaches  $v_s$  faster when compared to that of  $c = 1$ . Although the velocity profiles in Fig. 1(b) are noticeably different between  $c = 1$  and  $2$ , the current-voltage characteristics are not sensitively influenced by  $c$  (see also, Fig. 2(b) below). Thus, we focus on  $c = 1$  throughout Figs. 1(c) to (f).

Figs. 1(c) and 1(d) depict the normalised velocity and position profiles, respectively. For the case of  $\bar{v}_s = 10$ , the velocity does not saturate as compared to those of  $\bar{v}_s = 0.1$  and  $0.04$  within the time frame shown in Fig. 1(c) since it takes a longer time to reach a larger  $\bar{v}_s$ . Because the case of  $\bar{v}_s = 0.04$  rapidly saturates, the corresponding  $\bar{x}$  time-profile [Fig. 1(d)] is nearly a positive-sloped straight line, which is akin to that of a *constant-velocity* motion. In contrast, for the large- $\bar{v}_s$  case, the  $\bar{x}$  exhibits parabolic-like temporal profile which is akin to the case of *constant-acceleration* motion.

Fig. 1(e) shows the transit time ( $\bar{t}_{tr}$ ), i.e. the time taken for a charge carrier to travel the entire channel from  $x = 0$  to  $x = D$ , as a function of  $\bar{v}_s$ . Generally,  $\bar{t}_{tr}$  exhibits contrasting behaviours between low and high  $\bar{v}_s$ : (i)  $\bar{t}_{tr}$  decreases rapidly with increasing  $\bar{v}_s$  at smaller  $\bar{v}_s$

and (ii) the decreasing trend saturates at larger  $\bar{v}_s$ . Such contrasting behaviours can be explained as followed. At low  $\bar{v}_s$ , the carrier velocity is severely limited by the saturation effect. Increasing  $\bar{v}_s$  raises the ‘speed limit’ of the carrier. The  $\bar{t}_{tr}$  is thus reduced with increasing  $\bar{v}_s$ . As  $\bar{v}_s$  continues to increase to a larger value, the carriers reach the end of the channel before their velocity can reach  $\bar{v}_s$ . In this case, the transport is no longer  $\bar{v}_s$ -limited and  $\bar{v}_s$  has minimal influence on  $\bar{t}_{tr}$ , thus leading to the plateau at the high- $\bar{v}_s$  regime. We also note that an increasing  $\bar{\mu}$  appreciably decreases the  $\bar{t}_{tr}$  since larger mobility corresponds to an overall larger carrier velocity and hence a shorter transit time. The  $\bar{t}_{tr}$  decreases nearly monotonously with an increasing  $\bar{E}$  [Fig. 1(f)] since larger  $\bar{E}$  leads to a larger driving force for accelerating the carrier, thus resulting in an overall larger carrier velocity and, similarly, a shorter transit time. Furthermore, when the carrier velocity is strongly  $\bar{v}_s$ -limited (i.e. low  $\bar{v}_s$ ), the overall transit time is larger since the carrier velocity is rapidly capped by the lower  $\bar{v}_s$ .

By setting  $\bar{v}_s$  to be  $10^{10}$  so that the transport is nearly unaffected by the saturation effect, the  $\bar{J} - \bar{V}$  characteristics obtained for  $c = 1$  from our model is in excellent agreement with that obtained by a previous model of Darr et al<sup>27</sup> which does not include the velocity satura-

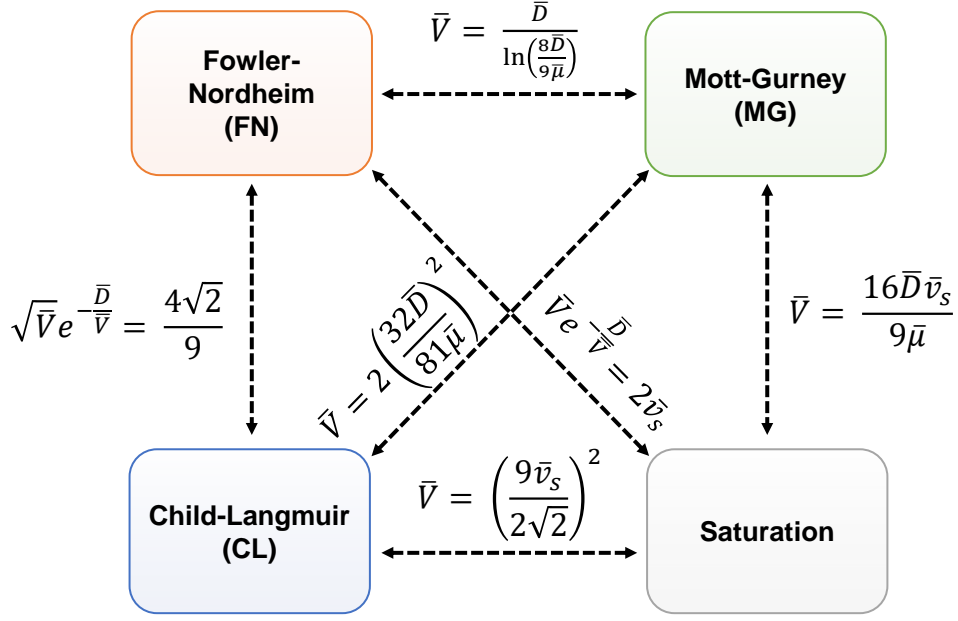


FIG. 3. Schematic diagram of all possible transitions between the four transport regimes and their respective transition boundary equations.

tion effect [Fig. 2(a)]. The velocity saturation effect on the  $\bar{J}-\bar{V}$  characteristics only becomes more prominent at lower  $v_s$ , leading to a velocity-saturated SCLC transport regime (i.e.  $\text{SCLC}_{\text{VS}}$ ) which is not captured by previous transitional model<sup>27</sup>. To investigate the significance of the fitting parameter,  $c$ , on the transport behaviour, the  $\bar{J}-\bar{V}$  characteristics for  $c = 1$  and  $2$  are plotted in Fig. 2(b). Apart from slight differences at low voltage, the  $\bar{J}-\bar{V}$  characteristics almost overlap between  $c = 1$  and  $c = 2$ . As the  $\bar{J}-\bar{V}$  characteristics are not sensitively influenced by  $c$ , electron and hole conductions are expected to yield similar  $\bar{J}-\bar{V}$  characteristics as well as the transitional behaviours. We thus focus on  $c = 1$  in the following section.

Figs. 2(c) to 2(e) show the  $\bar{J}-\bar{V}$  characteristics with different  $\bar{D}$ . Short-channel [Fig. 2(c)] and long-channel [Fig. 2(e)] devices exhibit contrasting  $\bar{J}-\bar{V}$  characteristics. At the short channel regime, a distinct CL-type SCLC ( $\text{SCLC}_{\text{CL}}$ ) occurs at the intermediate voltage regime. In this case, the carrier ballistically traverses across the entire channel before collisions can occur, thus leading to the vacuum-like  $\text{SCLC}_{\text{CL}}$ . In contrast, at the long-channel limit, the dominance of carrier scattering effect leads to a distinctive  $\text{SCLC}_{\text{MG}}$  at the intermediate regime. Interestingly, with intermediate-channel length ( $\bar{D} = 10^6$ ), the moderate-voltage regime exhibits both  $\text{SCLC}_{\text{MG}}$  and  $\text{SCLC}_{\text{CL}}$  scaling behaviours, thus simultaneous presence of both vacuum-like and solid-like characteristics of such device. Ultimately, the transport universally converges towards  $\text{SCLC}_{\text{VS}}$  at the high-voltage limit for all  $\bar{D}$ .

We now discuss the transitions between various transport processes by constructing the *nexus plots*, which can

be obtained by equating their respective current density equations (see Fig. 3 for schematic illustration of various transitional regimes). Fig. 4 reveals the rich transitional behaviours of the  $\bar{J}-\bar{V}$  characteristics across various device/material parameter spaces. For all channel lengths [Figs. 4(a) and (b)], the  $\text{SCLC}_{\text{VS}}$  is the ultimate transport process at high-voltage regime. At low-to-intermediate voltage,  $\text{SCLC}_{\text{CL}}$  ( $\text{SCLC}_{\text{MG}}$ ) dominates the short-channel (long-channel) devices – a behaviour consistent with the  $\bar{J}-\bar{V}$  characteristics in Fig. 2. For device with intermediate length, a more complex transition of  $\text{FN}-\text{SCLC}_{\text{MG}}-\text{SCLC}_{\text{CL}}-\text{SCLC}_{\text{VS}}$  with increasing voltage can occur, suggesting a solid-like to vacuum-like transport transition as observed in Fig. 2(d). Such effect is especially obvious in a low-mobility system [Fig. 4(a)] due to the prominence of carrier scattering and collisional effects.

The effect of  $\bar{v}_s$  is investigated in Figs. 4(c) and 4(d) at  $\bar{D} = 10^5$  and  $10^7$ , respectively. At low  $\bar{v}_s$ ,  $\text{SCLC}_{\text{VS}}$  is the only high-voltage process due to the severe carrier velocity limitation of  $\bar{v}_s$ , while  $\text{SCLC}_{\text{MG}}$  and/or  $\text{SCLC}_{\text{CL}}$  only emerge when the velocity saturation effect is relaxed (i.e. larger  $\bar{v}_s$ ). The effect of carrier mobility is investigated in Figs. 4(e) and 4(f) at  $\bar{v}_s = 0.1$  and  $\bar{v}_s = 1000$ , respectively. Contrary to the high- $\bar{v}_s$  case [Fig. 4(f)], the high-voltage transport is dominated by  $\text{SCLC}_{\text{VS}}$  at low  $\bar{v}_s$ . The  $\text{SCLC}_{\text{MG}}$  can, however, be resurrected in low-mobility devices, in which the carrier collisional and scattering effects can momentarily forbid the carrier velocity to saturate at the intermediate-voltage regime.

Finally, the transitional behaviours of three representative WBS, namely GaN, 6H-SiC and 4H-SiC, are shown in Figs. 5(a) to 5(c). As the transition boundary equa-

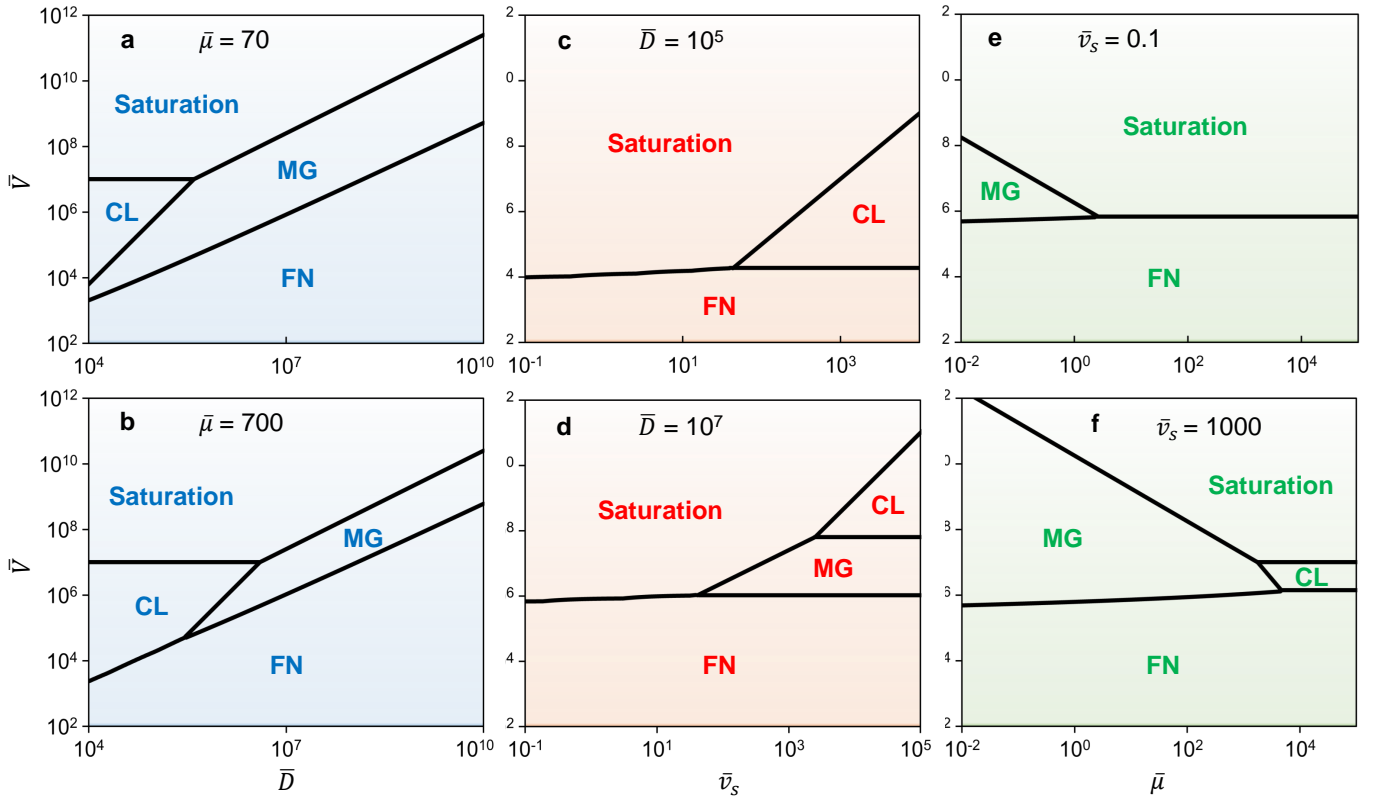


FIG. 4.  $\bar{V} - \bar{D}$  nexus plot at  $\bar{v}_s = 1000$  for (a)  $\bar{\mu} = 70$ , (b)  $\bar{\mu} = 700$ ;  $\bar{V} - \bar{v}_s$  nexus plot at  $\bar{\mu} = 700$  for (c)  $\bar{D} = 10^5$ , (d)  $\bar{D} = 10^7$  and  $\bar{V} - \bar{\mu}$  nexus plot at  $\bar{D} = 10^7$  for (e)  $\bar{v}_s = 0.1$ , (f)  $\bar{v}_s = 1000$ .

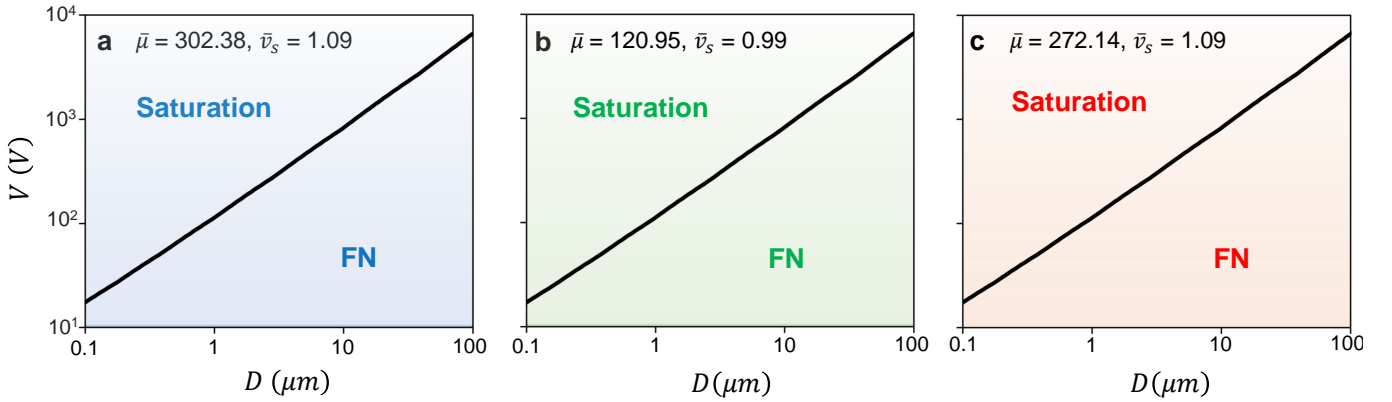


FIG. 5.  $V - D$  nexus plots for three common wide bandgap (WBG) semiconductors: (a) gallium nitride (GaN), (b) 6H-SiC and (c) 4H-SiC silicon carbide (SiC) polytypes. The value of the work function used to normalise both the mobility and saturation velocity is 0.2 eV.

tion of FN-SCLC<sub>VS</sub> is  $\bar{v}_s$ -dependent but  $\bar{\mu}$ -independent (see Fig. 3), the  $V$ - $D$  diagram exhibits similar behaviours for all three WBS (whose  $v_s$  values are similar). Here, FN transits directly into the velocity saturation regime without exhibiting any MG-type scaling, thus suggesting the dominance of SCLC<sub>VS</sub> over SCLC<sub>MG</sub>, thus illustrating the importance of SCLC<sub>VS</sub>, especially in the range of  $10^2 \sim 10^4$  V which is relevant to the operating voltage of typical WBS-based power electronics with sub- $\mu\text{m}$

channel length<sup>51</sup>.

In summary, we constructed a transitional transport model between field emission and space-charge-limited current with inclusion of the velocity saturation effect – an important behaviour especially in devices composed of (ultra)wide bandgap semiconductors and insulators. Using nexus plots spanning various device/material parameter spaces, the rich transitional behaviours between various conduction mechanisms were revealed. Us-

ing GaN, 6H-SiC and 4H-SiC as illustrative examples of WBG semiconductors, we showed that the velocity-saturated space-charge-limited current is the dominant conduction mechanism at typical sub- $\mu\text{m}$  device operating at  $10^2 \sim 10^4$  V, thus unraveling the importance of velocity saturation effect. Finally, we remark that our model can be further generalized to include the effects of thermionic<sup>52</sup>, quantum tunneling<sup>53,54</sup> and photo-induced emissions<sup>55,56</sup>, as well as unconventional electron emitters<sup>57–60</sup>.

## ACKNOWLEDGMENTS

This work is supported by the Singapore Ministry of Education Academic Research Fund Tier 2 (Award No. MOE-T2EP50221-0019) and the SUTD Kickstarter Initiatives (SKI) (Award No. SKI 2021.01.12).

## AUTHOR DECLARATIONS

### Conflict of Interest

The authors declare no conflict of interest.

### Author Contributions

**Kok Wai Lee:** Investigation (equal); Formal analysis (equal); Visualization (equal); Writing – original draft (lead); Visualization (lead); Writing – review and editing (supporting). **Yee Sin Ang:** Conceptualization (lead); Investigation (equal); Funding acquisition (lead); Formal analysis (equal); Supervision (lead); Visualization (supporting); Writing – original draft (supporting); Writing – review and editing (lead).

## DATA AVAILABILITY

The data that support the findings of this study are available from the corresponding author upon reasonable request.

- <sup>1</sup>P. Zhang, A. Valfells, L. K. Ang, J. W. Luginsland, and Y. Y. Lau, “100 years of the physics of diodes,” *Appl. Phys. Rev.* **4**, 011304 (2017).
- <sup>2</sup>P. Zhang, Y. S. Ang, A. L. Garner, Á. Valfells, J. Luginsland, and L. Ang, “Space-charge limited current in nanodiodes: Ballistic, collisional, and dynamical effects,” *J. Appl. Phys.* **129**, 100902 (2021).
- <sup>3</sup>C. Child, “Discharge from hot cathode,” *Phys. Rev. (Series I)* **32**, 492 (1911).
- <sup>4</sup>I. Langmuir, “The effect of space charge and residual gases on thermionic currents in high vacuum,” *Phys. Rev.* **2**, 450 (1913).
- <sup>5</sup>M. Zubair, A. Fatima, N. Raheem, Y. S. Ang, M. Q. Mehmood, and Y. Massoud, “Coordinate system invariant formulation of fractional-dimensional child-langmuir law for a rough cathode,” *Adv. Phys. Res.* **2**, 2200120 (2023).
- <sup>6</sup>N. Mott and R. Gurney, *Electronic Processes in Ionic Crystals* (Clarendon Press, Oxford, 1940).
- <sup>7</sup>M. A. Lampert, “Simplified theory of space-charge-limited currents in an insulator with traps,” *Phys. Rev.* **103**, 1648 (1956).
- <sup>8</sup>A. Rose, “Space-charge-limited currents in solids,” *Phys. Rev.* **97**, 1538 (1955).

- <sup>9</sup>P. Mark and W. Helfrich, “Space-charge-limited currents in organic crystals,” *J. Appl. Phys.* **33**, 205 (1962).
- <sup>10</sup>A. Grinberg, S. Luryi, M. Pinto, and N. Schryer, “Space-charge-limited current in a film,” *IEEE Trans. Electron Devices* **36**, 1162 (1989).
- <sup>11</sup>C. Y. Kee, Y. S. Ang, E.-P. Li, and L. Ang, “Analytical scaling of trap-limited current in 2-d ultrathin dielectrics,” *IEEE Trans. Electron Devices* **70**, 1527 (2022).
- <sup>12</sup>Y. Ang, M. Zubair, and L. Ang, “Relativistic space-charge-limited current for massive dirac fermions,” *Phys. Rev. B* **95**, 165409 (2017).
- <sup>13</sup>J. A. Röhr, “Direct determination of built-in voltages in asymmetric single-carrier devices,” *Phys. Rev. Appl.* **11**, 054079 (2019).
- <sup>14</sup>V. M. Le Corre, E. A. Duijnste, O. El Tambouli, J. M. Ball, H. J. Snaith, J. Lim, and L. J. A. Koster, “Revealing charge carrier mobility and defect densities in metal halide perovskites via space-charge-limited current measurements,” *ACS Energy Lett.* **6**, 1087 (2021).
- <sup>15</sup>J. Buhl, H. Lüder, and M. Gerken, “Injection-limited and space charge-limited currents in organic semiconductor devices with nanopatterned metal electrodes,” *Nanotechnology* **34**, 035202 (2022).
- <sup>16</sup>B. Karunakaran, S. Chung, E.-K. Suh, and D. Mangalaraj, “Dielectric and transport properties of magnetron sputtered titanium dioxide thin films,” *Phys. B: Condens. Matter* **369**, 129 (2005).
- <sup>17</sup>L. Partain and D. Liu, “Space-charge-limited current analysis of the leakage current and interface states of GaAs p/n diode solar cells,” *Appl. Phys. Lett.* **54**, 928 (1989).
- <sup>18</sup>E. A. Duijnste, V. M. Le Corre, M. B. Johnston, L. J. A. Koster, J. Lim, and H. J. Snaith, “Understanding dark current-voltage characteristics in metal-halide perovskite single crystals,” *Phys. Rev. Appl.* **15**, 014006 (2021).
- <sup>19</sup>O. Almora, G. J. Matt, A. These, A. Kanak, I. Levchuk, S. Shrestha, A. Osvet, C. J. Brabec, and G. Garcia-Belmonte, “Surface versus bulk currents and ionic space-charge effects in CsPbBr<sub>3</sub> single crystals,” *J. Phys. Chem. Lett.* **13**, 3824 (2022).
- <sup>20</sup>O. Almora, D. Miravet, M. García-Battle, and G. Garcia-Belmonte, “Ballistic-like space-charge-limited currents in halide perovskites at room temperature,” *Appl. Phys. Lett.* **119**, 242107 (2021).
- <sup>21</sup>J.-L. Zhang, Y.-X. Nan, H.-G. Li, W.-M. Qiu, X. Yang, G. Wu, H.-Z. Chen, and M. Wang, “A new wide bandgap organic semiconductor and its application in organic UV sensors with tunable response wavelength,” *Sens. Actuators B: Chem.* **162**, 321 (2012).
- <sup>22</sup>Y. Shi, Y. Tang, K. Yang, M. Qin, Y. Wang, H. Sun, M. Su, X. Lu, M. Zhou, and X. Guo, “Thiazolothienyl imide-based wide bandgap copolymers for efficient polymer solar cells,” *J. Mater. Chem. C* **7**, 11142 (2019).
- <sup>23</sup>Z.-X. Zhang, C. Li, Y. Lu, X.-W. Tong, F.-X. Liang, X.-Y. Zhao, D. Wu, C. Xie, and L.-B. Luo, “Sensitive deep ultraviolet photodetector and image sensor composed of inorganic lead-free Cs<sub>3</sub>Cu<sub>2</sub>I<sub>5</sub> perovskite with wide bandgap,” *J. Phys. Chem. Lett.* **10**, 5343 (2019).
- <sup>24</sup>I. Gaska, O. Bilenko, S. Smetona, Y. Bilenko, R. Gaska, and M. Shur, “Deep UV LEDs for public health applications,” *Int. J. High Speed Electron. Syst.* **23**, 1450018 (2014).
- <sup>25</sup>V. Adivarahan, G. Simin, G. Tamulaitis, R. Srinivasan, J. Yang, M. A. Khan, M. Shur, and R. Gaska, “Indium-silicon co-doping of high-aluminum-content AlGaIn for solar blind photodetectors,” *Appl. Phys. Lett.* **79**, 1903 (2001).
- <sup>26</sup>Y. Lau, Y. Liu, and R. Parker, “Electron emission: From the Fowler-Nordheim relation to the Child-Langmuir law,” *Phys. Plasmas* **1**, 2082 (1994).
- <sup>27</sup>A. M. Darr, A. M. Loveless, and A. L. Garner, “Unification of field emission and space charge limited emission with collisions,” *Appl. Phys. Lett.* **114**, 014103 (2019).
- <sup>28</sup>C. Chua, Y. S. Ang, and L. K. Ang, “Tunneling injection to trap-limited space-charge conduction for metal-insulator junction,”

- Appl. Phys. Lett. **121**, 192109 (2022).
- <sup>29</sup>A. M. Darr, C. R. Darr, and A. L. Garner, “Theoretical assessment of transitions across thermionic, field, and space-charge-limited emission,” *Phys. Rev. Res.* **2**, 033137 (2020).
- <sup>30</sup>C. Chua, C. Y. Kee, Y. S. Ang, and L. Ang, “Absence of space-charge-limited current in unconventional field emission,” *Phys. Rev. Appl.* **16**, 064025 (2021).
- <sup>31</sup>D. M. Caughey and R. Thomas, “Carrier mobilities in silicon empirically related to doping and field,” *Proc. IEEE* **55**, 2192 (1967).
- <sup>32</sup>B. Ridley, W. Schaff, and L. Eastman, “Hot-phonon-induced velocity saturation in gan,” *J. Appl. Phys.* **96**, 1499 (2004).
- <sup>33</sup>R. Shishir and D. Ferry, “Velocity saturation in intrinsic graphene,” *J. Phys.: Condens. Matter* **21**, 344201 (2009).
- <sup>34</sup>F. Roccaforte, F. Giannazzo, F. Iucolano, J. Eriksson, M. Weng, and V. Raineri, “Surface and interface issues in wide band gap semiconductor electronics,” *Appl. Surf. Sci.* **256**, 5727 (2010).
- <sup>35</sup>X. Chen, C. Chen, A. Levi, L. Houben, B. Deng, S. Yuan, C. Ma, K. Watanabe, T. Taniguchi, D. Naveh, *et al.*, “Large-velocity saturation in thin-film black phosphorus transistors,” *ACS Nano* **12**, 5003 (2018).
- <sup>36</sup>K. K. Smithe, C. D. English, S. V. Suryavanshi, and E. Pop, “High-field transport and velocity saturation in synthetic monolayer mos<sub>2</sub>,” *Nano Lett.* **18**, 4516 (2018).
- <sup>37</sup>O. S. Soboleva, V. V. Zolotarev, V. S. Golovin, S. O. Slipchenko, and N. A. Pikhin, “The effect of the carrier drift velocity saturation in high-power semiconductor lasers at ultrahigh drive currents,” *IEEE Trans. Electron Devices* **67**, 4977 (2020).
- <sup>38</sup>R. Woods-Robinson, Y. Han, H. Zhang, T. Ablekim, I. Khan, K. A. Persson, and A. Zakutayev, “Wide band gap chalcogenide semiconductors,” *Chem. Rev.* **120**, 4007 (2020).
- <sup>39</sup>A. Schenk, *Advanced Physical Models for Silicon Device Simulation* (Springer Science & Business Media, 1998).
- <sup>40</sup>A. Matallana, E. Ibarra, I. López, J. Andreu, J. Garate, X. Jordà, and J. Rebollo, “Power module electronics in hev/ev applications: New trends in wide-bandgap semiconductor technologies and design aspects,” *Renew. Sustain. Energy Rev.* **113**, 109264 (2019).
- <sup>41</sup>S. J. Bader, H. Lee, R. Chaudhuri, S. Huang, A. Hickman, A. Molnar, H. G. Xing, D. Jena, H. W. Then, N. Chowdhury, *et al.*, “Prospects for wide bandgap and ultrawide bandgap cmos devices,” *IEEE Trans. Electron Devices* **67**, 4010 (2020).
- <sup>42</sup>A. M. Loveless and A. L. Garner, “A universal theory for gas breakdown from microscale to the classical paschen law,” *Phys. Plasmas* **24**, 113522 (2017).
- <sup>43</sup>H. Wang, A. M. Loveless, A. M. Darr, and A. L. Garner, “Transitions between field emission and vacuum breakdown in nanoscale gaps,” *J. Vac. Sci. Technol. B* **40**, 062805 (2022).
- <sup>44</sup>R. H. Fowler and L. Nordheim, “Electron emission in intense electric fields,” *Proc. R. Soc. London, Ser. A* **119**, 173 (1928).
- <sup>45</sup>V. E. Dorgan, M.-H. Bae, and E. Pop, “Mobility and saturation velocity in graphene on sio<sub>2</sub>,” *Appl. Phys. Lett.* **97**, 082112 (2010).
- <sup>46</sup>B. H. Moon, H. Ji, J. J. Bae, and Y. H. Lee, “Temperature dependence of velocity saturation in a multilayer molybdenum disulfide transistor,” *Semicond. Sci. Technol.* **35**, 035030 (2020).
- <sup>47</sup>H. Chandrasekar, J. Cheng, T. Wang, Z. Xia, N. G. Combs, C. R. Freeze, P. B. Marshall, J. McGlone, A. Arehart, S. Ringel, *et al.*, “Velocity saturation in la-doped basno<sub>3</sub> thin films,” *Appl. Phys. Lett.* **115**, 092102 (2019).
- <sup>48</sup>L.-Y. Su and J. Huang, “Demonstration of radio-frequency response of amorphous igzo thin film transistors on the glass substrate,” *Solid-State Electron.* **104**, 122 (2015).
- <sup>49</sup>H. Dawson, “On the numerical value of  $\int_0^1 \text{hex } 2 \text{ dx}$ ,” *Proc. Lond. Math. Soc.* **1**, 519 (1897).
- <sup>50</sup>S. M. Sze, Y. Li, and K. K. Ng, *Physics of Semiconductor Devices* (John Wiley & Sons, 2021).
- <sup>51</sup>T. J. Flack, B. N. Pushpakaran, and S. B. Bayne, “Gan technology for power electronic applications: a review,” *J. Electron. Mater.* **45**, 2673 (2016).
- <sup>52</sup>E. L. Murphy and R. Good Jr, “Thermionic emission, field emission, and the transition region,” *Phys. Rev.* **102**, 1464 (1956).
- <sup>53</sup>P. Zhang, “Scaling for quantum tunneling current in nano- and subnano-scale plasmonic junctions,” *Sci. Rep.* **5**, 9826 (2015).
- <sup>54</sup>Y. Zhou, R. Ahsan, H. U. Chae, R. Kapadia, and P. Zhang, “Theoretical analysis of resonant tunneling enhanced field emission,” *Phys. Rev. Appl.* **20**, 014043 (2023).
- <sup>55</sup>K. L. Jensen, “General formulation of thermal, field, and photoinduced electron emission,” *J. Appl. Phys.* **102**, 024911 (2007).
- <sup>56</sup>K. L. Jensen, “Electron emission theory and its application: Fowler–Nordheim equation and beyond,” *J. Vac. Sci. Technol. B* **21**, 1528 (2003).
- <sup>57</sup>W. J. Chan, C. Chua, Y. S. Ang, and L. K. Ang, “Field emission in emerging two-dimensional and topological materials: A perspective,” *IEEE Trans. Plasma Sci.* , 1 (2022).
- <sup>58</sup>W. J. Chan, Y. S. Ang, and L. Ang, “Thermal-field electron emission from three-dimensional dirac and weyl semimetals,” *Phys. Rev. B* **104**, 245420 (2021).
- <sup>59</sup>Y. S. Ang, L. Cao, and L. K. Ang, “Physics of electron emission and injection in two-dimensional materials: Theory and simulation,” *InfoMat* **3**, 502 (2021).
- <sup>60</sup>Y. S. Ang, Y. Chen, C. Tan, and L. Ang, “Generalized high-energy thermionic electron injection at graphene interface,” *Phys. Rev. Appl.* **12**, 014057 (2019).